Heliyon 8 (2022) e08953

Contents lists available at ScienceDirect

Heliyon

journal homepage: www.cell.com/heliyon

Research article

Using egg ovalbumin to synthesize pure α-Fe_2O_3 and cobalt doped α-Fe_2O_3: structural, morphological, optical and photocatalytic properties

Soufiane Hmamouchi [a], Ahmed El Yacoubi [a,b,*], Brahim Chafik El Idrissi [a]

[a] Advanced Materials and Process Engineering Laboratory, Faculty of Sciences, Ibn Tofail University, Kenitra, Morocco
[b] Laboratory of Applied Chemistry and Environment, Mineral Solid Chemistry Team, Mohamed First University, Oujda, Morocco

ARTICLE INFO

Keywords:
Hematite α-Fe_2O_3
Co doped α-Fe_2O_3
Egg white ovalbumin
Optical and photocatalytic properties
Methylene blue
Photo-adsorption isotherms

ABSTRACT

Nanoparticles of undoped hematite (α-Fe_2O_3) and Co doped α-Fe_2O_3 were prepared by a simple, green, and cost-efficient process using Co and Fe chlorides and freshly isolated hen egg white. Several techniques of characterization, such as differential thermal and thermogravimetric analysis (DTA/TG), Fourier transform infrared spectroscopy (FTIR), scanning electron microscopy (SEM), EDS analysis, X-ray diffraction analysis (XRD), and Ultra-violet Visible (UV–Vis) analysis were applied. The incorporation of Co particles into the hematite matrix limits the growth of the α-Fe_2O_3 crystalline grain and favours the apparition of γ-Fe_2O_3 phase. SEM analysis reveals that there are no significant morphological differences among α-Fe_2O_3 and Co-α-Fe_2O_3 particles, whereas the XPS analysis confirms the existence of Fe and Co particles in the as-prepared samples. The optical study shows a slight reduction of band gap energy for Co doped α-Fe_2O_3 compared to the non-doped α-Fe_2O_3, which has shown enhanced visible light adsorption performance. On the other hand, the α-Fe_2O_3 and Co-α-Fe_2O_3 nano-photocatalysts with an average crystallite size of 21 and 43 nm respectively, were used to remove the Methylene Blue (MB) dye from aqueous solutions after being exposed to visible light. In a mechanistic study, the radicals $OH^{\bullet}$ and $^{\bullet}O_2^-$ were shown to be important in the degradation of MB dye. To optimise the effective parameters on MB dye degradation, the experimental parameters applied in the adsorption experiments, such as pH, photocatalyst dosage, contact time, and temperature, were tested. The optimal conditions were determined as pH = 12, photocatalyst dosage = 0.2 g/L. Degradation efficiency in the optimal conditions is 91.8 % after 120 min of irradiation. The pseudo-first and second orders were used to model the kinetic data. The removal of MB using α-Fe_2O_3 and Co-α-Fe_2O_3 photocatalysts matched well with pseudo-second-order reaction kinetics. Furthermore, the thermodynamic study reveals that MB dye adsorption on the Co-Fe2O3 absorbent was an endothermic and spontaneous process.

1. Introduction

Because of their adjustable surface morphology, distinctive crystal structure, and intrinsic catalytic properties, transition metal oxides have received a lot of technological and scientific attention [1]. Among these, hematite α-Fe_2O_3 has recently been discovered as an important alternative and promising candidate for solar photocatalysis, which can degrade organic dyes with excellent photo-oxidation activity [2, 3]. Iron oxide α-Fe_2O_3 (Hematite), the most stable iron oxide with a rhombo-hexagonal structure, has received extensive research, especially in photocatalytic applications, due to its low-cost, non-toxicity, exceptional stability, excellent anti-ferromagnetic characteristics, simple recovery [4, 5], and appropriate band gap energy Eg (2.0–2.3 eV). These properties allow it to absorb more than half of the visible light (λ > 600 nm), collect up to 40% of the energy from the incident solar spectrum, and remain stable in the vast majority of aqueous solutions (pH > 3) [6]. Cobalt ferrites, among the various ferrites, have recently attracted interest, due to its excellent chemical stability, extremely high electrical resistivity, excellent mechanical hardness, and significant permeability at high frequencies as well as to being low-cost [7, 8]. Contaminated water is major problem these days. the photocatalytic method has attracted the interest of researchers for reducing the content of dye molecules in used water before it is discharged into the environment. Methylene blue (MB) dye is widely utilized in textile industries such as dyeing and printing. It is also employed in medical field because of its antifungal characteristics. However, over use of MB dye can cause serious dietary and health

* Corresponding author.
E-mail address: elyacoubi6ahmed@gmail.com (A. El Yacoubi).

https://doi.org/10.1016/j.heliyon.2022.e08953
Received 16 October 2021; Received in revised form 12 December 2021; Accepted 9 February 2022

problems such as vomiting, gastrointestinal distress [9]. Therefore, it is necessary to develop low-cost, eco-friendly and effective materials for the degradation of many dyes from wastewater. As one of the potential photocatalysts with high photocatalytic reactivity, α-Fe_2O_3 appears to be an essential material to remove several dyes and organic pollutants [10]. Generally, the photocatalytic performance of such a photocatalyst can be affected by several factors, including exposed surface facets, crystalline phase, porous structure, specific surface area, and morphological characteristics [11, 12]. According to the literature, α-Fe_2O_3 powders in various shapes, such as nanoparticles [13] nanorods [14] nanoflowers [15] nanodisks [16] Nanospheres [17] and spindles [18] have been prepared by different techniques, including hydrothermal [19], solvothermal [20], sol-gel [21] and co-precipitation [22]. To choose a simple process for the synthesis of nano-ferrites, the use of low-cost and nontoxic precursors seems to be the key issue. Moreover, because of the link between biological structures and inorganic molecules, green synthesis is one of the top interesting subjects of nanomaterials research [23]. The gelling, foaming, and emulsifying properties of egg white proteins are well recognized [24]. It has been used to shape materials as a binder or gel. Although it is less proficient, the use of egg white facilitates the process and offers another alternative method to synthesize the nano-crystalline particles with low-effective method. To the best of our knowledge, there is no method that provides the production of pure α-Fe_2O_3 and Co-α-Fe_2O_3 particles using egg ovalbumin.

The current findings show the synthesis of α-Fe_2O_3 and Co-α-Fe_2O_3 nanoparticles at a relatively low temperature by a simple, ecologically, and cost-effective process using $CoCl_2{\cdot}6H_20$, $FeCl_3{\cdot}6H_2O$ and using, for the first-time, hen egg white as a precursor. The structural, optical, and morphological properties of α-Fe_2O_3 and Co-α-Fe_2O_3 nanoparticles were studied by DTA/TGA, XRD, FTIR, UV-visible spectroscopy, and SEM. The photocatalytic efficiency of α-Fe_2O_3 and Co-α-Fe_2O_3 was evaluated by examining the degradation of MB dye under visible light irradiation.

2. Materials and methods

2.1. α-Fe_2O_3 and Co-α-Fe_2O_3 synthesis

All substance reagents used in present work were of analytical grade and utilized with no supplementary purification. The α-Fe_2O_3 and Co-α-Fe_2O_3 NPs were elaborated, for the first time, by an aqueous co-precipitation process using a hen egg white as a source of oxygen. Iron (III) chloride hexahydrate ($FeCl_3.6H_2O$, >97%) and cobalt chloride's hexahydrate ($CoCl_2.6H_2O$, 98%) were provided by Sigma Aldrich and were used as received.

In a conventional method, the freshly extracted hen ovalbumin was first mixed and homogenized with distilled water under vigorous agitation at 500 rpm for 30 min to get a well-homogenized solution (Solution A). Subsequently, the desired amounts of metal precursors $FeCl_3.6H_2O$ and $CoCl_2.6H_2O$ were first dissolved in distilled water (Solution B) and added dropwise to the as-prepared ovalbumin solution. For the synthesis of Co- α-Fe_2O_3 NPs, 1.189g of $CoCl_2.6H_2O$ and 2.703g of $FeCl_3.6H_2O$ were added to solution A to achieve an atomic ratio of Co/Fe = 0.5. Throughout the synthesis process, the pH of the mixture is not controlled. The resultant yellow suspension was then heated for 2h, under continuous stirring (500rpm), in a hot plate at 80 °C. Finally, the pale-yellow suspension was filtered and washed, for several occasions, by means of warm distilled water to eliminate any potential impurities or any possible contaminants and dried overnight at 100 °C. The obtained deep red samples were crushed into powder with agate mortar and annealed at 550 °C for 2h and then decreased to ambient temperature to get α-Fe_2O_3 and Co- α-Fe_2O_3 NPs. Figure 1 shows a quick overview of the synthesis of undoped and Co doped α-Fe_2O_3 photocatalysts.

2.2. Characterization techniques

The different crystalline phases present in the as prepared powders were identified by a Shimadzu 6100 Diffractometer, with a wavelength λ of copper Kα radiation equal to 1.5406 Å, operating at 40 kV in the scan range of 20–70° with a step scan of 0.02°. Infrared patterns were recorded in the range of 350–4000 cm^{-1} with an attenuated total reflection ATR-FTIR spectrometer. The morphological properties and surface compositions of elaborated samples were carried out by a scanning electron microscopy (SEM) coupled with Energy dispersive system X-ray micro-spectrometer (EDAX). To understand the thermal behaviour of the involved samples, the thermogravimetric analysis (TG/DTG) was investigated using a Shimadzu DTG-60 thermal analyser with a heating rate of 10 °C/min.

2.3. Photocatalytic activity assessment of the prepared photocatalysts

The photocatalytic features of α-Fe_2O_3 and Co-α-Fe_2O_3 nano-photocatalysts were performed by degrading methylene blue (MB) dye in an aqueous medium when exposed to visible light (36 LED Lamp). The vertical distance between the LED lamp and the dye solution, in axial opposition, is kept constant and equal to 10 cm. To reach the adsorption-desorption balance, the photocatalyst powder and solution dye mixture was placed, under magnetic agitation (800 rpm), in the dark for 30 min. The absorption values were collected at the wavelength corresponding to the most extreme adsorption of the used inorganic dye (λ_{max} = 664 nm). Typically, the desired amount of the prepared photocatalyst was scattered into 50 mL of MB dye aqueous solution (1 g/L), under constant stirring (700 rpm), and irradiated by a visible light lamp for the required time. The result suspensions were periodically centrifuged to remove the photocatalyst powder from the dye solution. The degradation rates (%) of the photocatalyst were carried out using UV-visible 2005 spectrophotometer (Eq. (1)).

$$\text{Degradation efficiency} = \frac{A_0 - A}{A_0} * 100\ \% \quad (1)$$

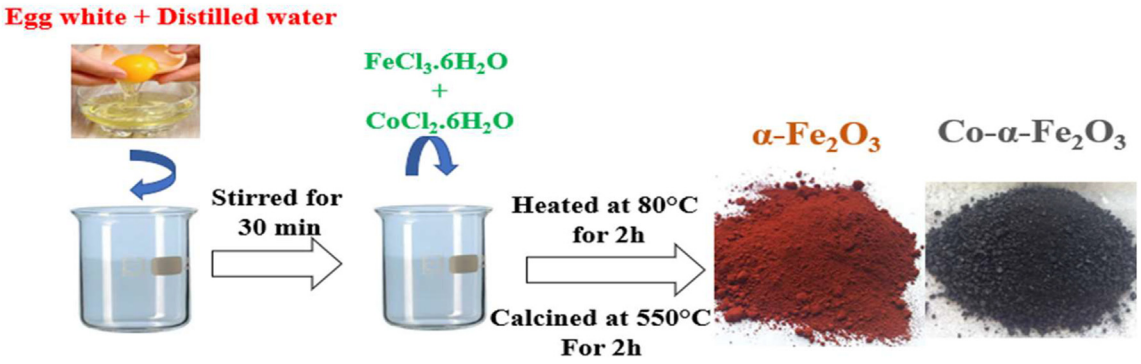

Figure 1. Schematic representation of the synthesis of α-Fe_2O_3 and Co-α-Fe_2O_3 photocatalysts.

Where A_0 and A are the initial and the final absorbance after irradiation process, respectively.

3. Results and discussion

3.1. Characterization

The XRD patterns of hematite α-Fe_2O_3 and Co-doped hematite Co-α-Fe_2O_3 nano-photocatalysts are shown in Figure 2. Among these, the two samples were switched well with the rhombohedral space group of α-Fe_2O_3 phase (R-3c (167), a = b = 0.50356 Å, c = 1.37489 Å, JCPDS card N°: 33–0664), which illustrates that the presence of Co particles does not affect the α-Fe_2O_3 crystal type. Table 1 summarizes all the x-ray diffraction peaks for α-Fe_2O_3 specimen. In the case of the Co doped sample, additional very weak peaks can be detected at 30.16 and 43.35°. Such peaks correspond to γ-Fe_2O_3 phase, which is thermodynamically less stable. From these results, it may be deduced that Co^{2+} ions doping limits the proliferation of α-Fe_2O_3 crystals and promotes the growth of γ-Fe_2O_3 phase. Other authors have reported the same observations in the literature [25, 26]. In addition, due to the existence of Co, the diffraction peaks of the Co doped powder hematite α-Fe_2O_3 have been moved to lower angles in the pattern, compared to those of the pure α-Fe_2O_3 powder, confirming the successful insertion of Co ions into the pure hematite lattice. These angular variations are generally synonymous with a modification of the distance between two diffraction planes due to the incorporation of Co ions in the α-Fe_2O_3 lattice (different ionic radius). The average crystallite size of particle was determined using the well-known Scherer formula (Eq. (2)) from the full width at half maximum (FWHM) of XRD patterns [27].

$$D = \frac{0.9\,\lambda}{\beta\ \cos\theta} \tag{2}$$

where D is the average crystallite size (nm), β is the peak's broadening or FWHM (rad), λ is the Cu-Kα X-ray wavelength and θ is the Bragg-position of the concerning peak determined from the XRD pattern.

The peak width FWHM at low-angle is more relevant to estimating the grain size from XRD data. Hence, the particle size of nanoparticles was computed using the maximum intensity peak (104). According to the preceding method, the average size of the α-Fe_2O_3 and Co- α-Fe_2O_3 nanoparticles was 43 and 21 nm, respectively. It is clear that the crystalline size of α-Fe_2O_3 decreases significantly with the insertion of Co ions, which indicates that the Co particles limit the growth of the crystalline grain.

FT-IR spectroscopy is a characterization technique, based on the adsorption of infrared radiation by the analysed material, which gives the different functional groups present in the sample. Figure 3 depicts the FT-IR spectra for pure α-Fe_2O_3 and Co-α-Fe_2O_3 samples from 360 to 4000 cm^{-1}. The absorption bands for the two FT-IR spectra are quite similar. The spectra show two characteristic bands at 427 cm^{-1} and 519 cm^{-1} which correspond to the Fe-O stretching vibration mode of iron oxide. The strong and medium intense adsorption bands at 519 cm^{-1} and 439 cm^{-1} arise from the intrinsic stretching vibrational mode ν_1 of the Fe-O liaison and the bending vibration ν_2 of the O-Fe-O [28], respectively.

Table 1. Peak positions and Miller indices of hematite α-Fe_2O_3 photocatalyst.

Peak position 2θ (°)	Miller indices (facet direction)
24.21	(012)
33.21	(104)
35.72	(110)
40.93	(113)
49.54	(024)
54.14	(116)
57.60	(122)
62.50	(214)
64.07	(300)

Figure 4 displays only the thermal behavior of Co-α-Fe_2O_3 photocatalyst from room temperature to 800 °C. The decomposition process starts with the vaporization of hydrated water (a minor weight loss), followed by a series of TG steps (major weight loss) due to the decomposition of remaining organic moieties present in the egg-white after the synthesis step. Weight loss and the very large endothermic peaks at-110° and 205 °C are synonyms of the loss of adsorbed and surface-bound water molecules. The two exothermic DTA peaks located at 280 and 324 °C can be ascribed to the decomposition of the organic substance. The large exothermic DTA at 462 °C can be attributed to the Co-α-Fe_2O_3 formation. There was no major weight loss observed after 570 °C. The formation of Co-α-Fe_2O_3 nanocrystalline was confirmed by a weak endothermic DTA peak at 540 °C which corresponded to the crystallization process of the hematite α-Fe_2O_3 phase, as confirmed by XRD and FT-IR analysis.

Figure 5 illustrates the SEM images of α-Fe_2O_3 and Co-α-Fe_2O_3 photocatalyst materials. After analysing the SEM images, it is apparent that the grain size of both samples is inhomogeneous and gets agglomerated in some cases. The loss of nanostructure-stabilizing ions by washing with water is thought to be the cause of the agglomeration [29]. As can be shown in Figure 5, SEM images of Co-doped α-Fe_2O_3 samples (Figure 5a and b) were substantially clearer than those of undoped α-Fe_2O_3 samples, which might be attributed to enhanced electrical conductivity of α-Fe_2O_3 nanoparticles after Co doping [30, 31]. SEM images reveal also that the crystallites do not have a regular and uniform shape. By comparing the micrographs, we can clearly see that there are no significant

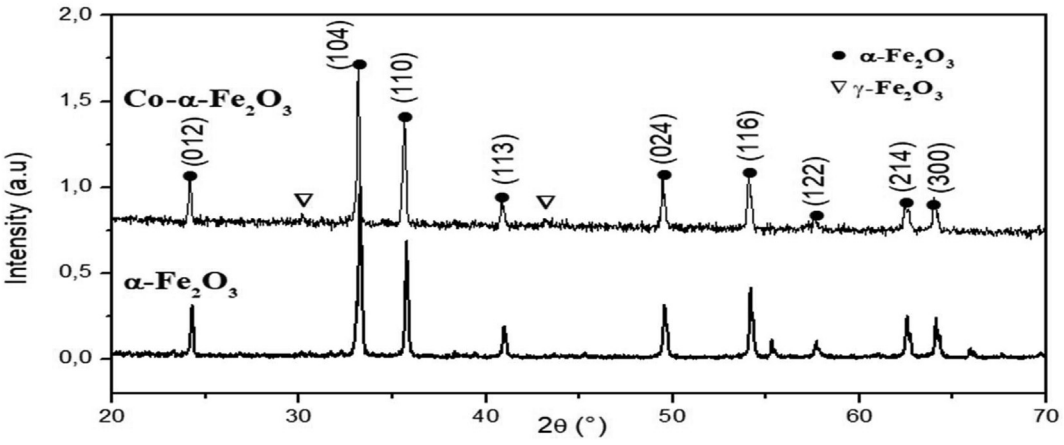

Figure 2. XRD patterns of α-Fe_2O_3 and Co-α-Fe_2O_3 photocatalysts.

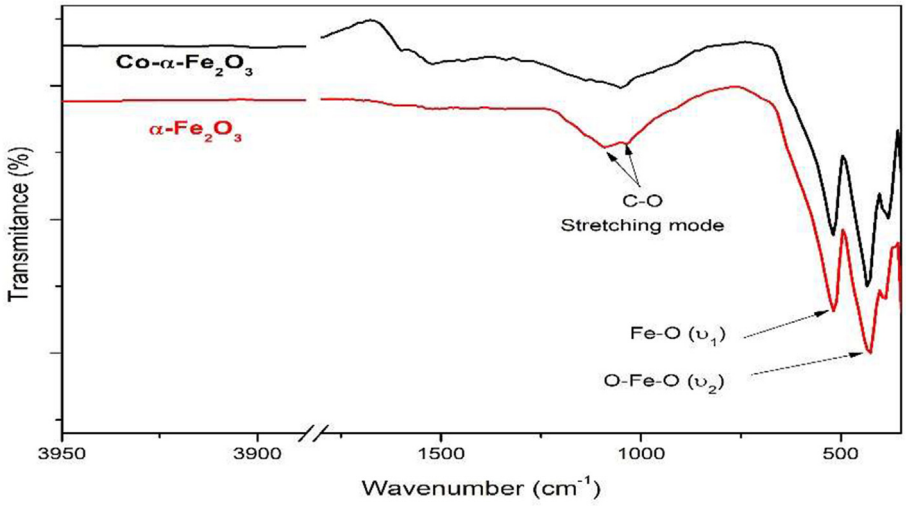

Figure 3. FTIR spectra of α-Fe_2O_3 and Co-α-Fe_2O_3 samples calcined at 550 °C for 2 h.

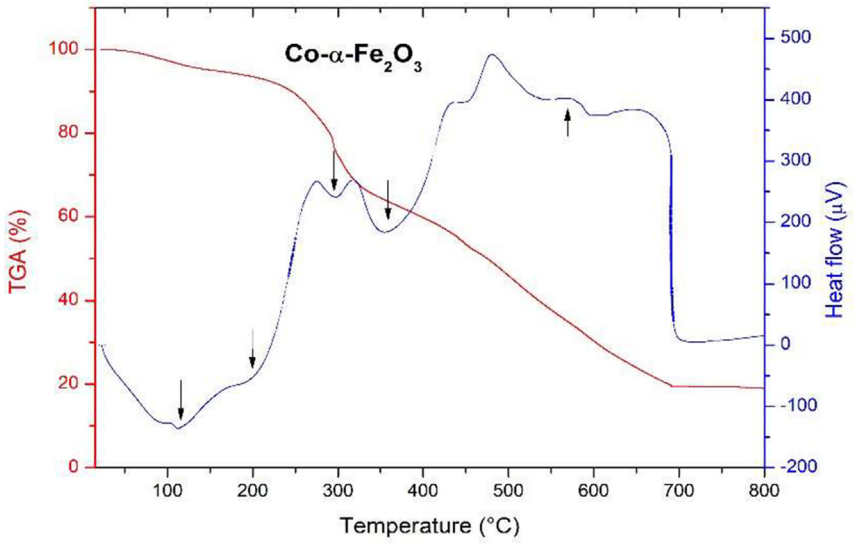

Figure 4. Thermal analysis DTA/TG of Co doped α-Fe_2O_3 nanoparticles.

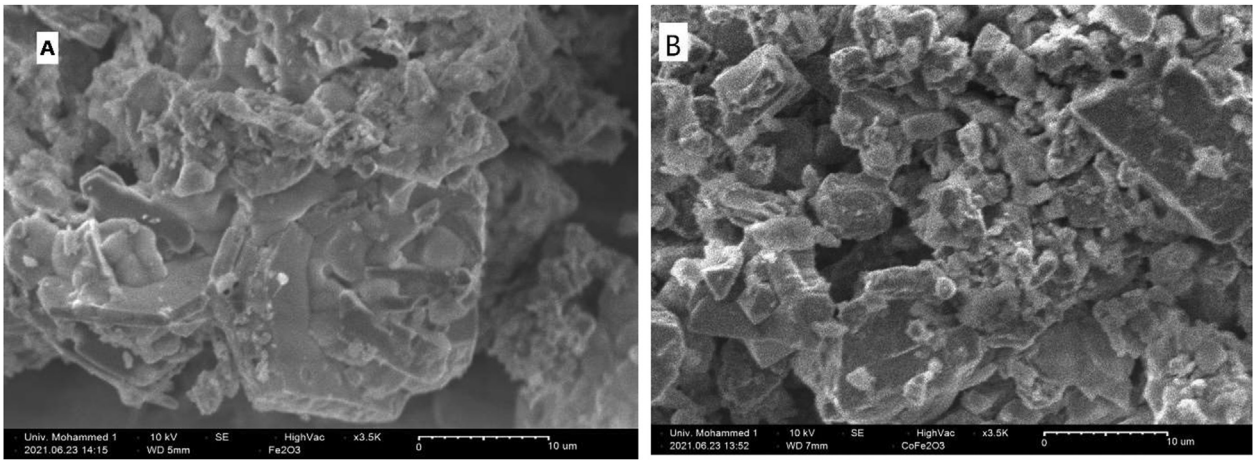

Figure 5. SEM images of the as-prepared photocatalysts materials A) α-Fe_2O_3 B) Co-α-Fe_2O_3.

morphological differences among α-Fe_2O_3 and Co-α-Fe_2O_3 specimens, indicating that the morphology of α-Fe_2O_3 is not influenced by cobalt doping. Grain sizes estimated by the XRD technique are significantly smaller than those seen by SEM. This difference in grain size could be explained by the fact that the SEM analysis gives only the average particle size of the analyzed surface, which means that each grain is constituted by the aggregation of many nanocrystals, whereas the XRD technique focuses on the crystallite size of single particles. Satheesh et al. report the same [22]. Furthermore, the composition of the synthesized photocatalysts was carried out by EDX analysis. Figure 6 depicts the EDX patterns of α-Fe_2O_3 and Co-α-Fe_2O_3 materials. All the elements constituting the hematite phase appear at their corresponding keV energy values.

3.2. Optical property

Extrapolation from the absorption may be used to calculate the optical bandgap (E_g) for α-Fe_2O_3 and Co-α-Fe_2O_3 nanoparticles employing the well-known Tauc's equation [32] (Eq. (3)):

$$(\alpha h\upsilon)^n = A(h\upsilon - E_g) \quad (3)$$

Where α, E_g, A, hυ and n are the absorption coefficient, bandgap energy, optical constant, energy of emitted light, and a constant characterizing the type of the electronic transition [33], i.e., n = 2 for direct transition and n = 1/2 for indirect transition [34]. Undoped and Co^{2+} doped α-Fe_2O_3 show direct as well as indirect transition. Figure 7a, b show the absorption edge $(\alpha h\upsilon)^n$ versus photon energy hυ for the two ways of transition (direct and indirect) and the obtained band gap energy is shown in Table 2. The valence band (E_{VB}) and conduction band (E_{CB}) potentials for α-Fe_2O_3 and Co- α-Fe_2O_3 were estimated by using Eqs. (4) and (5), respectively [3].

$$E_{VB} = \chi - E_e + \frac{1}{2}.E_g \quad (4)$$

$$E_{CB} = E_{VB} - E_g \quad (5)$$

Where χ, Ee and Eg correspond to the absolute Mulliken electronegativity (=5.87 eV), the energy of free electrons on the hydrogen scale (=4.5 eV) and the system band gap energy. The calculated E_{VB} and E_{CB} edge potentials were: E_{VB} = 2,51 eV; E_{CB} = 0.23 eV and E_{VB} = 2.38eV; E_{CB} 0.355 eV for α-Fe_2O_3 and Co-α-Fe_2O_3, respectively.

The indirect transition is caused by the excitation of forbidden spin Fe^{3+} 3d→3d, whereas the direct transition is related to the transfer of charge O^{2-} 2p→ Fe^{3+} 3d. According to the literature, the estimated bandgap values of direct and indirect transitions of α-Fe_2O_3 vary in the range of 2–2.6 eV [25, 35] and 1.38–2.09 [36] respectively. Our results are consistent with previous reports. Compared with the non-doped hematite specimen, the band gap of the Co doped α-Fe_2O_3 was slightly reduced, which indicates that the Co^{2+} doping process affects the conduction band edge of α-Fe_2O_3, leading to enhanced visible light absorption properties. However, supplementary density states, in the bandgap of α-Fe_2O_3 material, would be generated by the coupling interaction effect between the co dopant and Fe atoms, and consequently shift the conductive band minimum upward, closer to the redox level of H_2O/H_2 couple [34]. Since α-Fe_2O_3 is an excellent absorber of visible light irradiation, the insertion of Co particles could only slightly decrease the bandgap of α-Fe_2O_3 under these conditions [34].

3.3. Photocatalytic properties evaluation

The photocatalytic performances of the nano-photocatalyst samples were investigated by the degradation of methylene blue (MB) molecules after exposure to visible-light. As an initial starting point, the experiments were carried out at pH = 12 with a MB concentration of 10 mg/L and with a photocatalyst concentration of 0.2 g/L of MB solution. To estimate the self-photodegradation of MB dye effect, a control experiment was conducted under irradiation of visible light without a photocatalyst phase, which revealed that there was no remarkable change in MB concentration. Figure 8 depicts the absorbance of different times of MB dye in the presence of α-Fe_2O_3 and Co-α-Fe_2O_3 nano-photocatalysts. All UV–visible absorption spectra show a maximum absorbance at 664 nm. With the increase in irradiation time, the absorption intensity at 664 nm decreases confirming the degradation of the MB dye. At the beginning of reaction (t = 0) the color of the MB solution changed from navy blue to light blue. However, as adsorption increased, it became practically transparent, indicating that most of the MB molecules present in the dye solution were adsorbed by the α-Fe_2O_3 and Co-α-Fe_2O_3 photocatalysts. The adsorption efficiency of photocatalysts raise quickly in the initial 10 min, and reached to 71.3 and 82.3% for undoped and Co^{2+} doped α-Fe_2O_3 respectively, to stabilise after 120 min of visible irradiation at 90.2 and 91.8% respectively.

3.3.1. Effect of pH

Industries discharge waste water containing organic compounds at various pH values. Therefore, it is important to study the efficacy of catalysts towards the removal of dyes at different pH. The experiment was investigated at different pH values ranging from 5 to 13 for constant MB concentration (10 mg/L) and photocatalyst loading of 1 g/L. Figure 9 illustrates the photodegradation percentage of MB as a function of pH. As shown in Figure 8, with increasing pH, the efficiency of the photocatalysts for MB degradation increased and exhibited high color removal at pH = 12, after 60 min of irradiation, for both α-Fe_2O_3 and Co-α-Fe_2O_3 photocatalysts. This result may be explained by the effect of the adsorbent surface charge and point of zero charge (pzc) of α-Fe_2O_3 [37].

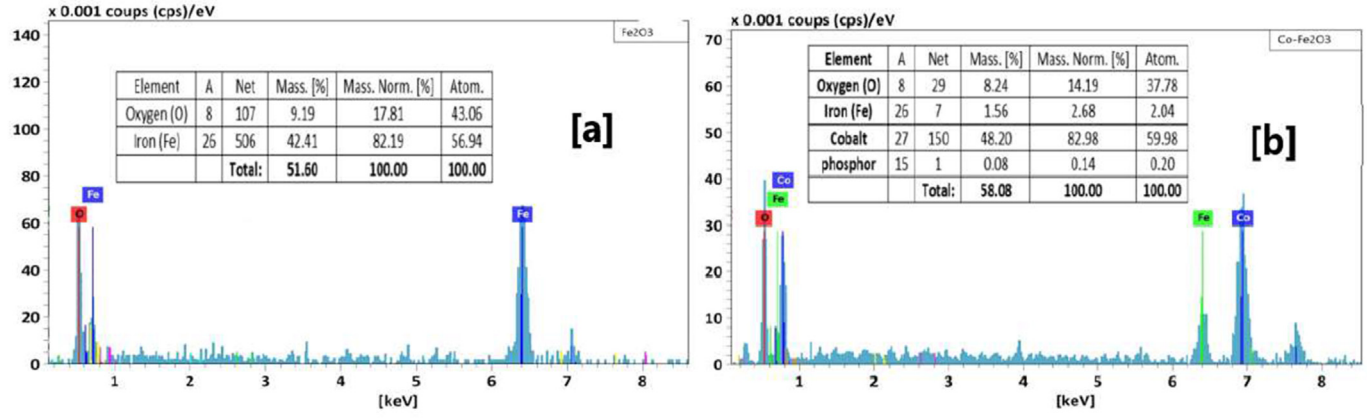

Figure 6. Energy dispersive spectrum of [a] α-Fe_2O_3 and [b] Co-α-Fe_2O_3 photocatalysts.

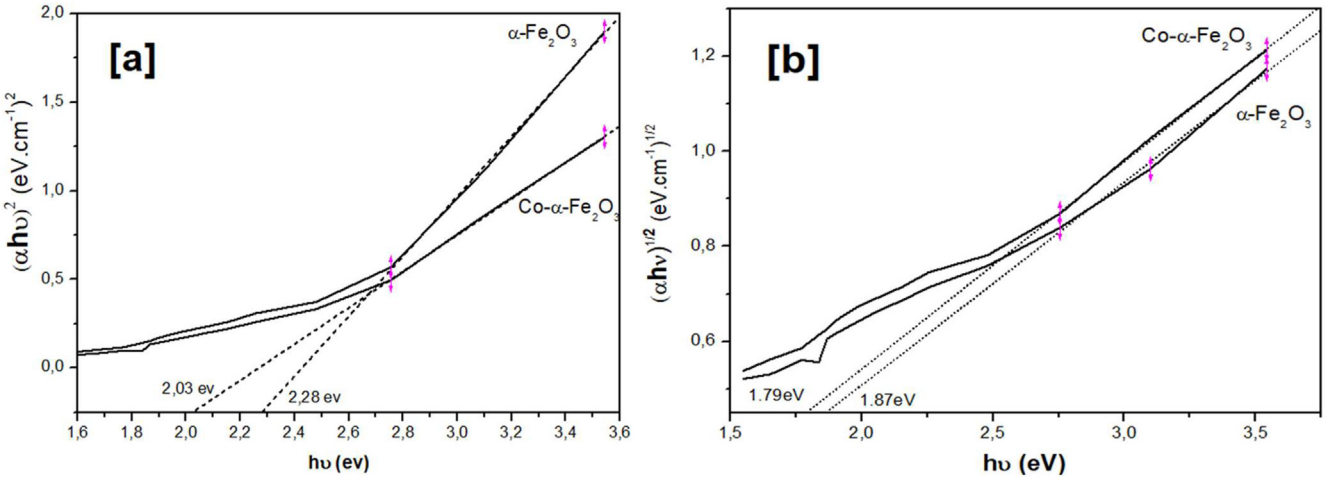

Figure 7. Tauc plots of α-Fe_2O_3 and Co-α-Fe_2O_3 for [a] direct transition [b] indirect transition.

Table 2. Bandgap values of α-Fe_2O_3 and Co-α-Fe_2O_3 photocatalysts.

	Bandgap (eV)	
	Direct transition	Indirect transition
α-Fe_2O_3	2.28	1.87
Co-α-Fe_2O_3	2.03	1.79

Indeed, the absorbent surface charge is mostly controlled by the pH_{PZC}. From the pzc, given in Figure 10, pH_{pzc} (α-Fe_2O_3) = 5.3. Therefore, the surface of α-Fe_2O_3 becomes positively charged below the pH_{pzc} and becomes gradually more negatively charged above the pH_{pzc}. The weak MB adsorption at low pH may be due to electrostatic repulsion forces between positively loaded MB (cationic dye) and positively loaded adsorption sites [38]. When the mixture pH increases, the contact surface of α-Fe_2O_3 becomes more negatively charged, and an important electrostatic attraction force is developed between the cationic molecules of MB dye and the negatively charged α-Fe_2O_3 surface, which in turn enhances adsorption efficiency [39].

3.3.2. Photocatalyst dosage effect

As is well known, the degradation efficiency is widely influenced by the amount of catalyst dispersed in the pollutant solution. The photodegradation tests were performed by varying the catalyst dosages (α-Fe_2O_3 and Co-α-Fe_2O_3) ranging from 0.1 to 1.4 g/L at pH = 12 and keeping the MB concentration (10 mg/L) constant. Figure 11 illustrates the photodegradation efficiency of MB with photocatalyst dosage. According to Figure 11, the photodegradation efficiency beyond 0.2 g/L decreases as the photocatalytic dosage increases. The photodegradation percentage of MB is 82.88 and 85.71% at 0.2 g/L of α-Fe_2O_3 and Co-α-Fe_2O_3 respectively. The same phenomenon was observed by other researchers [20, 22, 40]. When the catalyst dosage is optimised (0.2 g/L), more active sites become available on the catalyst's surface. It also absorbs enough light to create sufficient active •OH radicals on the α-Fe_2O_3 and Co-α-Fe_2O_3 surfaces. This is assigned to the agglomeration of photocatalyst particles, which decreases the number of active sites on the surface area [20]. On the other hand, the high stirring speed with a high photocatalyst dose may limit the penetration of light into solution, leading to a decrease in the total photoactivated volume by affecting the electron-hole formation, hence the photocatalytic efficiency decreases.

3.3.3. Contact time effect

Contact time is a key issue in the absorption process because it relates to the amount of sorbent fixed and contact time. It is used to estimate how long it will take to reach sorption–desorption equilibrium. The effect of contact time on the removal of MB dye is shown in Figure 12. The adsorption process began with a higher adsorption rate and decreased progressively with increasing adsorption time to finally achieve equilibrium after 60 min of adsorption. At the start of absorption phenomena, the high adsorption rate might be attributed to the availability of too many unoccupied active adsorption sites on the α-Fe_2O_3 and Co-α-Fe_2O_3

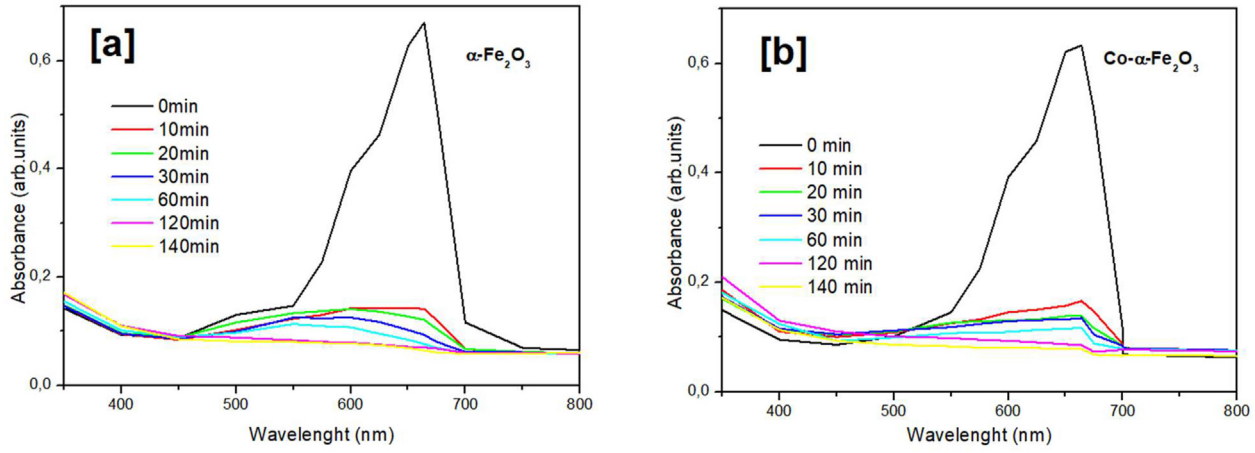

Figure 8. UV-Visible absorbance spectra of [a] α-Fe_2O_3 [b] Co-α-Fe_2O_3 photocatalysts.

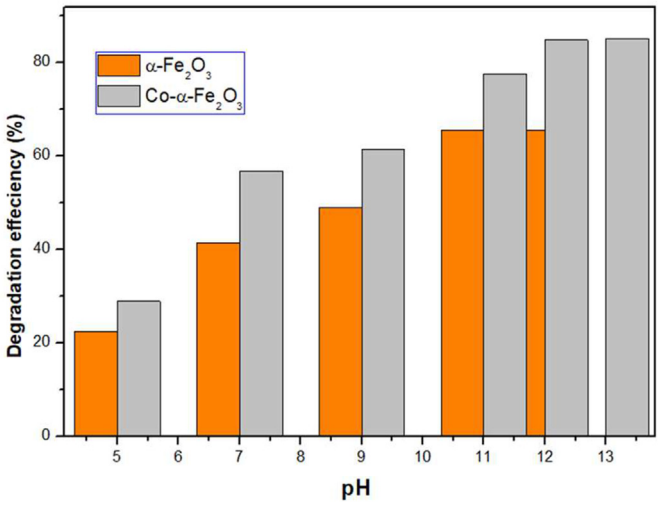

Figure 9. Degradation efficiency of the two prepared photocatalysts for MB dye solution.

surfaces, which could be used, leading to a rapid adsorption rate. As adsorption time increases, active adsorption sites are increasingly occupied by MB molecules, causing a lower adsorption rate. Furthermore, adsorbed and non-adsorbed MB ions create powerful repulsive forces, making the rest of the sites increasingly difficult to occupy until achieving an equilibrium state [38]. The low adsorption rate at the end of experiments suggests the eventual monolayer formation of MB on the photocatalyst surface [41]. A quick comparison of the current results with previously published experiments based on α-Fe_2O_3 doping is shown in Table 3.

3.3.4. Effect of the temperature

Temperature is an important physical parameter that can change the adsorption capacity of the adsorbent. This effect on the adsorption of MB dye on Co-α-Fe_2O_3 was investigated from 298 to 328 K under stirring for 30 min. Figure 13 shows the adsorption capacity increased from 43.025 to 46.93 mg g^{-1}, when the temperature was increased from 298 to 328 K, which indicates that the adsorption is an endothermic process. This may be due to the strengthening of the attractive forces between MB and the active sites on the Co-α-Fe_2O_3 surface.

3.3.5. Photo-adsorption kinetics

The pseudo first order (PFO) kinetic model of Lagergren [45] is given by the Eq. (6):

$$\ln(q_e - q_t) = \ln q_e - k_1 t \quad (6)$$

where, q is the amount of MB adsorbed (mg/g) at: equilibrium state q_e and time t q_t, while k_1 represents the first order rate constant (min^{-1}). A linear plot of $\ln(q_e\text{-}q_t)$ versus t provides a relationship between k_1 and q_e,

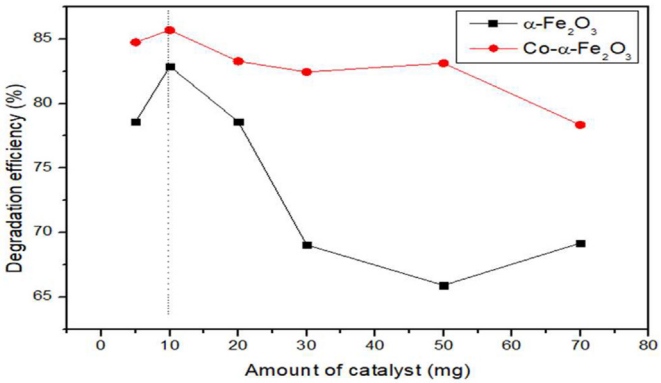

Figure 11. Degradation efficiency with photocatalysts dosage.

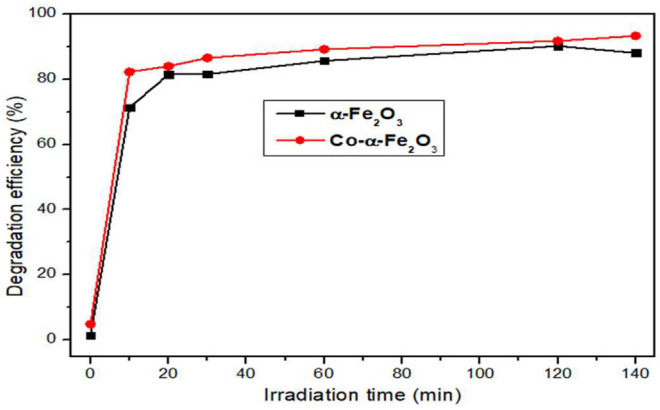

Figure 12. Degradation efficiency of MB dye with irradiation time.

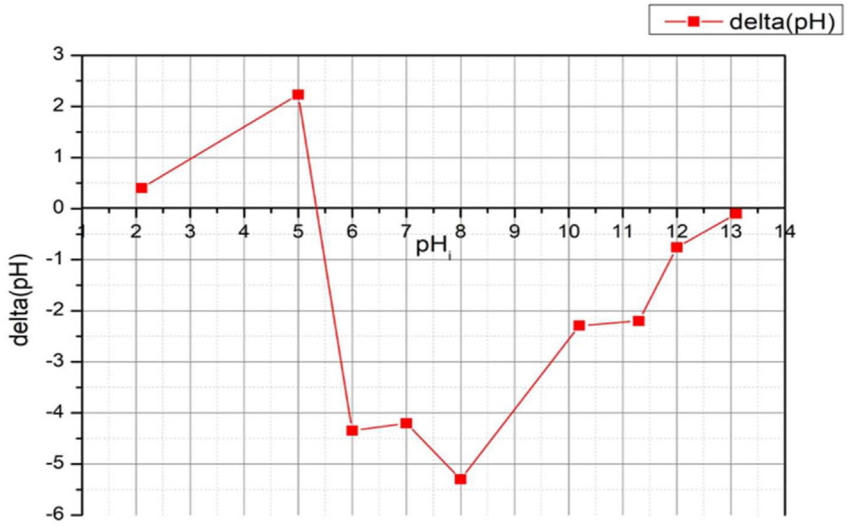

Figure 10. Point of zero charge (PZC) graph of α-Fe_2O_3.

Table 3. A Comparative study of the present results with those reported in the literature.

	Synthesis method	Crystallite's size (nm)	Particle's morphology	Energy band gap (eV)	Removal rate (%)	Ref.
Co doped α-Fe_2O_3	Sol gel	13–15	Spherical	α-Fe_2O_3: 1.93 Co-α-Fe_2O_3: 1.83	–	[8]
Co doped α-Fe_2O_3	Hydrothermal	31–65	Rhombohedral	–	92% (60 min) MB dye	[42]
Co^{3+} substituted Fe^{3+} in hematite	Combination of precipitation and calcination	10–28	Nanorods Nanoneedles (in high substitution rate)	α-Fe_2O_3: 2.14 Co-α-Fe_2O_3: 2.03–2.08	30–35% (180 min) Dye: RhB	[43]
(M = Cu, Ni and Co) doped α-Fe_2O_3	Co-precipitation	16–26	Spherical	α-Fe_2O_3: 1.93 Co-α-Fe_2O_3: 1.83 Cu-α-Fe_2O_3: 1.72 Ni-α-Fe_2O_3: 1.51	98.05% (90 min) Dye: Acid Red-27	[22]
(M = Cu, Mn, Cr, Nb, Mo, Ti, V,Zn, Ni and Co) doped α-Fe_2O_3	Hydrothermal	100–200	dodecahedron	Direct: 1.97–2.01 Indirect: 2.04–2.08	–	[34]
Sn doped α-Fe_2O_3	combination of hydrothermal, co-precipitation and calcination	10–143	Nanorods nanoellipsoids nanocuboids	Sn-α-Fe_2O_3: 2.10–2.18	60% (30 min) Dye: RhB	[44]
Present work	Co-precipitation	21–43	No regular shape	α-Fe_2O_3: 2.28 Co-α-Fe_2O_3: 2.03	92% (120 min) Dye; MB	–

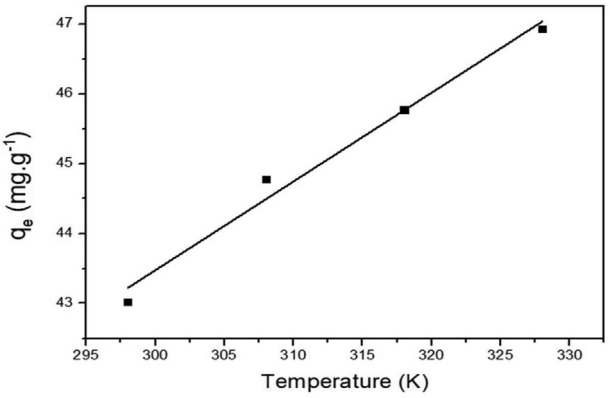

Figure 13. Temperature effect on the adsorption of MB dye on Co-α-Fe_2O_3 absorbent surface.

which can be calculated from the slope and the intercept of the affine function $\ln(q_e\text{-}q_t) = f(t)$.

The linearized form of the pseudo second order (PSO) rate equation is given by the Eq. (7):

$$\frac{dq}{[q_e - q_t]^2} = k_2 dt \tag{7}$$

Where q_e and q_t are the adsorbed quantities of adsorbate system per unit mass of sorbent at equilibrium state and at any time (mg g^{-1}), respectively, and k_2 is the PSO rate constant (g mg^{-1} min^{-1}). Taking into consideration the boundary conditions (t = 0 to t = t and q = 0 to q = q_t), and after integration of the previous equation, the linear form of the PFO model expression is as follows (Eq. (8) and (9)):

$$\frac{1}{(q_e - q_t)} - \frac{1}{q_e} = k_2\, t \tag{8}$$

This linear form can be written as:

$$\frac{t}{q_t} = \frac{1}{k_2 q_e^2} + \frac{t}{q_e} \tag{9}$$

A plot of t/q_t versus t provides a linear relationship, from which the kinetic model constants of PSO (q_e and k_2) are calculated from the slope and interception. Figure 14 illustrates the PFO and PSO kinetic plots for α-Fe_2O_3 and Co-α-Fe_2O_3 photocatalysts.

Table 4 shows the results of applying MB adsorption data on α-Fe_2O_3 and Co-α-Fe_2O_3 to the PFO and PSO kinetic models. As can be shown in Table 4 and Figure 14, the PSO kinetic model has a higher correlation factor ($R^2 > 0.999$) than the PFO kinetic model ($R^2 = 0.634$). These results showed that the MB adsorption on the α-Fe_2O_3 and Co-α-Fe_2O_3 photocatalysts closely follows the PSO kinetics. Sivalingam et al. [46] and Koyuncu et al. [47] report the same results.

3.3.6. Adsorption thermodynamics

The thermodynamic parameters, such as the variation in Gibbs free energy (ΔG^0, kJ mol^{-1}), variation in enthalpy (ΔH^0, kJ mol^{-1}), and variation in entropy (ΔS^0, kJ mol^{-1} K^{-1}), were calculated for Co-α-Fe_2O_3 adsorption experiments at four different temperatures (25, 35, 45, and 55 °C), using the Eqs. (10), (11), and (12):

$$\Delta G^0 = -\,RT \ln(K_d) \tag{10}$$

$$\Delta G^0 = \Delta H^0 - T\Delta S^0 \tag{11}$$

$$\ln(Kd) = \frac{\Delta S^0}{R} - \frac{\Delta H^0}{RT} \tag{12}$$

Where $K_d = q_e/C_e$ is the adsorption distribution coefficient or thermodynamic equilibrium constant, R is a constant of gas (8.314 J mol^{-1} K^{-1}) and T is a temperature (K). Using the Eq. (12), ΔH^0 and ΔS^0 were calculated from the slop and the intercept of K_d versus 1/T graph. The computed thermodynamics parameters are shown in Table 5. As can be shown, the ΔG^0 values were all negative, implying a spontaneous adsorption process, and the adsorption of MB dye on the Co-α-Fe_2O_3 sample was a physisorption in nature [48, 49]. In addition, as the temperature increased, ΔG^0 became more negative, suggesting that the process was spontaneous. Moreover, the adsorption process is generally chemisorption when ΔH^0 is between 40 kJ mol^{-1} and 800 kJ mol^{-1}, and physisorption when ΔH^0 is less than 40 kJ mol^{-1} [50]. In our case, the ΔH^0 value was positive and less than 40 kJ mol^{-1}, which indicates that the adsorption of MB dye was physisorption in nature and an endothermic process. On the other hand, the Positive ΔS^0 value for MB adsorption showed an increase in randomness at the solid-solution interface, which might be attributable to the electrostatic attraction of the MB adsorbate, replacing the surface hydration shell [49].

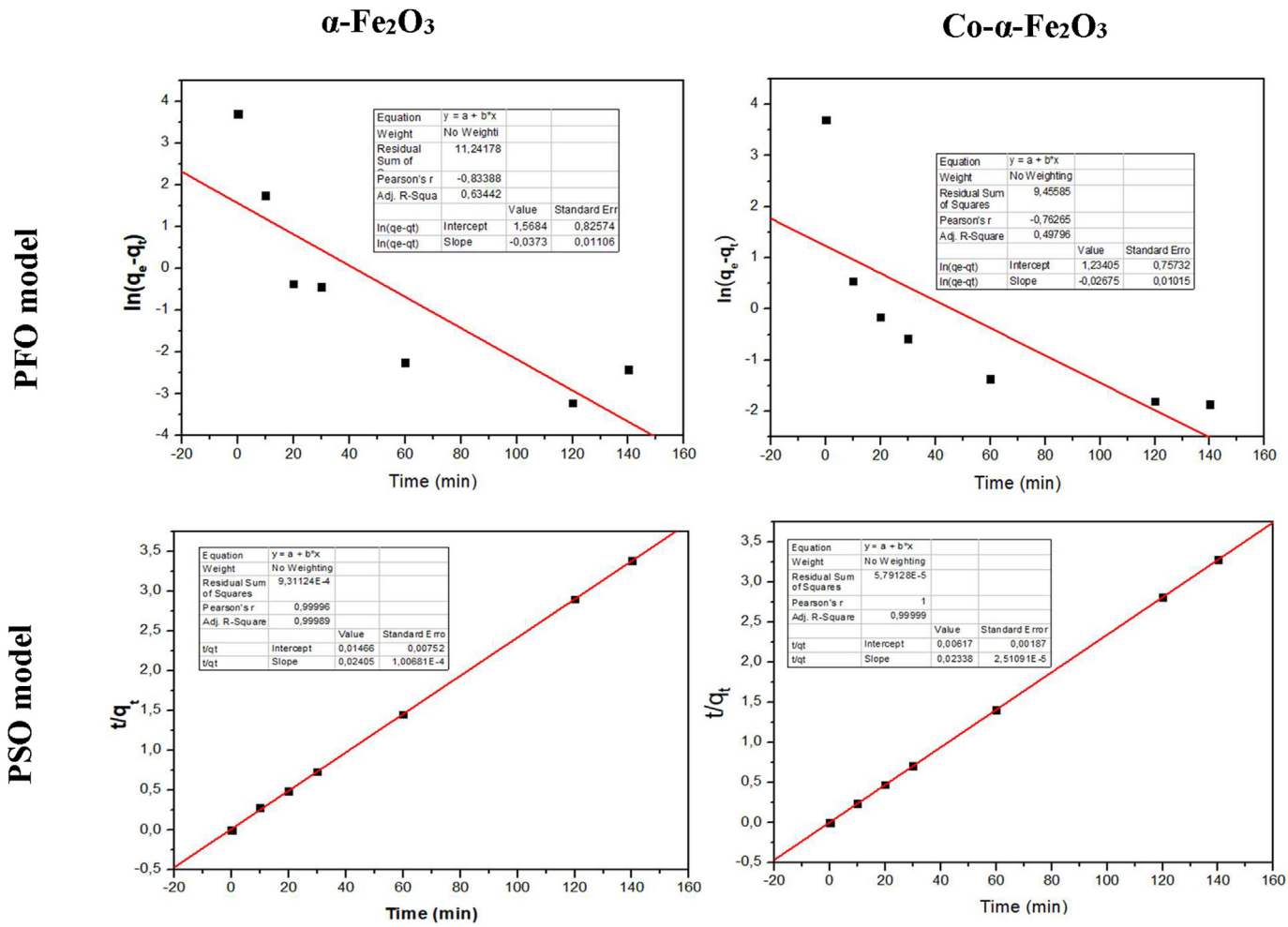

Figure 14. PFO and PSO kinetic plots for the adsorption of α-Fe_2O_3 and Co-α-Fe_2O_3.

Table 4. Kinetic parameters of α-Fe_2O_3 and Co- α-Fe_2O_3 photocatalysts.

	PFO model			PSO model			
	q_e (mg g^{-1})	K_1 (g mg^{-1}. min^{-1})	R^2	Q_e (mg g^{-1})	q_e^2	K_2 (g mg^{-1}. min^{-1})	R^2
α-Fe_2O_3	4,79	3,1. 10^{-4}	0,63442	41,3206	1707,3925	3,99. 10^{-2}	0,9998
Co-α-Fe_2O_3	3,43	2, 16. 10^{-4}	0,4979	42,77	1829,4	8,85. 10^{-2}	0,9999

Table 5. Thermodynamic data for the adsorption of MB by Co doped hematite photocatalyst.

Sample	T (K)	lnK_d	ΔG^0 (kJ. Mol^{-1})	ΔH^0 (kJ mol^{-1})	ΔS^0 (kJ. Mol^{-1} K^{-1})
Co-α-Fe_2O_3	298	3.53	-8.75	20.80	0.99
	308	3.84	-9.83		
	318	4.04	-10.69		
	328	4.31	-11.77		

4. Photocatalytic mechanism

In the photocatalytic reaction, a surface charge-transfer process is widely required [19]. Figure 15 illustrates the proposed mechanism for the MB photodegradation by α-Fe_2O_3 and Co-α-Fe_2O_3 photocatalysts. During the irradiation step on α-Fe_2O_3 and Co-α-Fe_2O_3 photocatalysts, the excited electrons (e^-) jump from valence band VB to conduction band CB, and leaving holes (h^+_{VB}) at photocatalyst VB (Eq 13). Photogenerated holes can combine with water molecules H_2O adsorbed on the photocatalyst surface to create highly reactive radicals of hydroxyl ($OH^\bullet$) and H^+ ions (Eq.14), which have been considered to be the main active species in the photocatalytic mechanism [51]. In addition, the h^+_{VB} in the VB can also combine with OH^- ions, present in the alkaline medium, to produce ($OH^\bullet$) radicals (eq.15). The photogenerated e^- from CB (e^-_{CB}) reacts with the dioxygen (O_2) dissolved in the dye solution and yields superoxide radical ($^\bullet O_2^-$) (Eq.16). $OH^\bullet$ and $^\bullet O_2^-$ attack MB molecules on or near the surface of photocalysts (Eqs. (17) and (18)).

$$\alpha\text{-}Fe_2O_3 + h\upsilon \rightarrow \alpha\text{-}Fe_2O_3 + h^+_{VB} + e^-_{CB} \quad (13)$$

$$\alpha\text{-}Fe_2O_3\text{-}(h^+_{VB}) + H_2O \rightarrow OH^\bullet + H^+ + \alpha\text{-}Fe_2O_3 \quad (14)$$

$$\alpha\text{-}Fe_2O_3\text{-}(h^+_{VB}) + OH^- \rightarrow OH^\bullet + \alpha\text{-}Fe_2O_3 \quad (15)$$

$$\alpha\text{-}Fe_2O_3\text{-}(e^-_{CB}) + O_2 \rightarrow {}^\bullet O_2^- \quad (16)$$

$$OH^\bullet + MB \rightarrow CO_2 + H_2O \text{ (degradation process)} \quad (17)$$

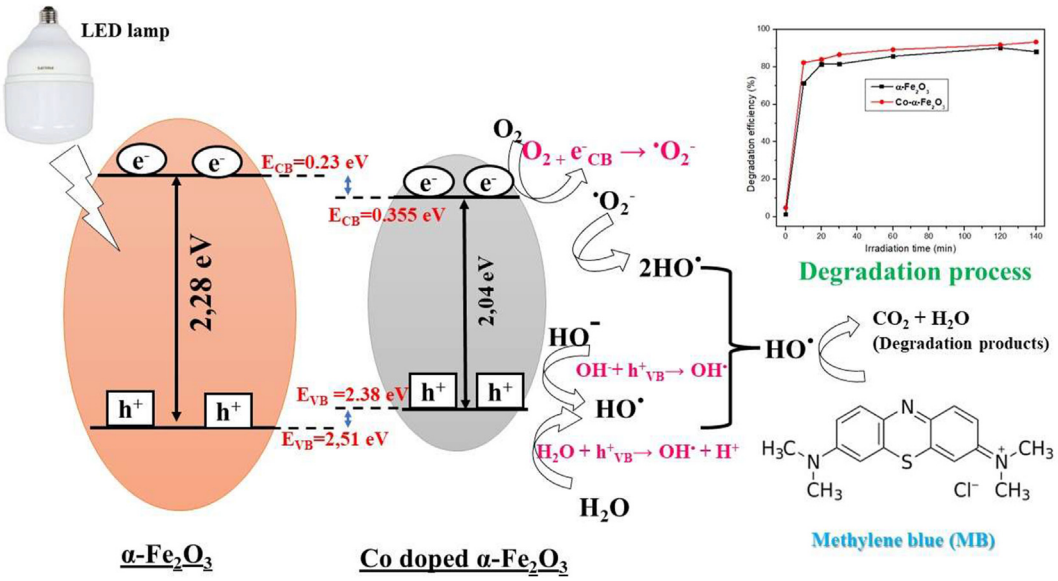

Figure 15. The proposed mechanism for the MB photodegradation by α-Fe_2O_3 and Co-α-Fe_2O_3 photocatalysts.

$$^{\bullet}O_2^- + MB \rightarrow CO_2 + H_2O \text{ (degradation process)} \quad (18)$$

Therefore, in the presence of H_2O, the super oxide radicals $^{\bullet}O_2$ released during the irradiation process can react with holes to give $OH^{\bullet}$ radicals and H_2O_2, or react with H^+ ions to form O_2 and H_2O_2 as shown by Eqs. (19) and (20) [16, 52, 53]:

$$^{\bullet}O_2^- + h^+_{VB} + 2H_2O \rightarrow 2OH^{\bullet} + H_2O_2 \quad (19)$$

$$2^{\bullet}O_2^- + 2H^+ + 2H_2O \rightarrow O_2 + H_2O_2 \quad (20)$$

Furthermore, unlike α-Fe_2O_3, Co-α-Fe_2O_3 has a Co^{2+} impurity energy level that traps electrons, lowering the electron-hole pair recombination rate [40]. This is the main explanation for the slight improvement in photocatalytic activity of Co-α-Fe_2O_3 compared to non-doped α-Fe_2O_3 [25].

5. Conclusion

In light of this study, α-Fe_2O_3 and Co doped α-Fe_2O_3 nanoparticles were successfully synthesised by a green and low-cost chemical route using freshly extracted egg white for the first time. The thermal, structural, vibrational, morphological, and optical properties were analysed by DTA/TG, XRD, FTIR, SEM, EDS and UV-Vis analysis. XRD data of annealed samples (at 550 °C) revealed that the Co doping mainly produces the secondary phase γ- Fe_2O_3. The lattice parameters and crystallite size were affected by this doping. The EDX analysis reveals the existence of Co and Fe particles in the prepared specimens. UV-visible optical characterization of α-Fe_2O_3 and Co-α-Fe_2O_3 nanoparticles revealed direct and indirect band gap energy. The band gap values of Co doped α-Fe_2O_3 are decreased compared to undoped α-Fe_2O_3 nanoparticles. The removal efficiency of methylene blue (MB) dye using a photocatalysis process has been studied. The obtained results indicate that the prepared samples have demonstrated high adsorption efficiency. It was also found that doping by Co^{2+} slightly enhanced the photocatalytic degradation activity of α-Fe_2O_3 nanoparticles. The photoadsorption kinetics agreed well with the pseudo-second order model. Thermodynamic study indicates an endothermic and spontaneous process of adsorption.

Declarations

Author contribution statement

Soufiane Hmamouchi: Performed the experiments; Analyzed and interpreted the data.

Ahmed El Yacoubi: Analyzed and interpreted the data; Wrote the paper.

Brahim Chafik El Idrissi: Conceived and designed the experiments; Analyzed and interpreted the data; Contributed reagents, materials, analysis tools or data; Wrote the paper.

Funding statement

This research did not receive any specific grant from funding agencies in the public, commercial, or not-for-profit sectors.

Data availability statement

Data will be made available on request.

Declaration of interests statement

The authors declare no conflict of interest.

Additional information

No additional information is available for this paper.

References

[1] J. Hu, et al., Hydrogen evolution electrocatalysis with binary-nonmetal transition metal compounds, J. Mater. Chem. 5 (13) (2017) 5995–6012.

[2] J.R. Jesus, R.J.S. Lima, K.O. Moura, J.G.S. Duque, C.T. Meneses, Anisotropic growth of α-Fe2O3 nanostructures, Ceram. Int. 44 (4) (Mar. 2018) 3585–3589.

[3] A. Ahmed, M. Usman, B. Yu, Y. Shen, H. Cong, Sustainable fabrication of hematite (α-Fe2O3) nanoparticles using biomolecules of Punica granatum seed extract for

unconventional solar-light-driven photocatalytic remediation of organic dyes, J. Mol. Liq. 339 (Oct. 2021) 116729.
[4] C. Chen, et al., Porous Fe2O3 nanotubes with α-γ phase junction for enhanced charge separation and photocatalytic property produced by molecular layer deposition, Appl. Catal. B Environ. 248 (Jul. 2019) 218–225.
[5] X. Dai, G. Lu, Y. Hu, X. Xie, X. Wang, J. Sun, Reversible redox behavior of Fe2O3/TiO2 composites in the gaseous photodegradation process, Ceram. Int. 45 (10) (Jul. 2019) 13187–13192.
[6] R. Schrebler, et al., Electrochemically grown self-organized hematite nanotube Arrays for photoelectrochemical water splitting, J. Electrochem. Soc. 161 (14) (Oct. 2014) H903–H908.
[7] B.A. Aldar, R.K. Pinjari, N.M. Burange, Electric and dielectric behavior of Ni-Co-Cd ferrite, IOSR J. Appl. Phys. 6 (4) (2014) 23–26.
[8] S. James Jeyaseelan, K. Parasuraman, S. Johnson Jeyakumar, M. Jothibas, B. Arunkumar, Synthesizing and characterization of cobalt doped Fe2O3 nanoparticles and their magnetic behaviour, INFOKARA Res. 9 (1) (2020) [Online]. Available: https://infokara.com/gallery/52-jan-3494.pdf.
[9] R. Begum, J. Najeeb, A. Sattar, K. Naseem, A. Irfan, A.G. Al-Sehemi, Z.H. Farooqi, Chemical reduction of methylene blue in the presence of nanocatalysts: a critical review, Rev. Chem. Eng. 36 (6) (2020) 749–770.
[10] C.N.C. Hitam, A.A. Jalil, A review on exploration of Fe2O3 photocatalyst towards degradation of dyes and organic contaminants, J. Environ. Manag. 258 (Mar. 2020) 110050.
[11] A.A. Fauzi, et al., Altering fiber density of cockscomb-like fibrous silica–titania catalysts for enhanced photodegradation of ibuprofen, J. Environ. Manag. 227 (Dec. 2018) 34–43.
[12] M. Rosales, T. Zoltan, C. Yadarola, E. Mosquera, F. Gracia, A. García, The influence of the morphology of 1D TiO2 nanostructures on photogeneration of reactive oxygen species and enhanced photocatalytic activity, J. Mol. Liq. 281 (May 2019) 59–69.
[13] P. Sharma, R. Kumar, S. Chauhan, D. Singh, M.S. Chauhan, Facile growth and characterization of α-Fe_2O_3 nanoparticles for photocatalytic degradation of methyl orange, J. Nanosci. Nanotechnol. 14 (8) (Aug. 2014) 6153–6157.
[14] X. Xie, et al., Synthesis of hollow microspheres constructed with α-Fe2O3 nanorods and their photocatalytic and magnetic properties, J. Alloys Compd. 477 (1–2) (May 2009) 90–99.
[15] S. Zeng, et al., Facile route for the fabrication of porous hematite nanoflowers: its synthesis, growth mechanism, application in the lithium ion battery, and magnetic and photocatalytic properties, J. Phys. Chem. C 112 (13) (Mar. 2008) 4836–4843.
[16] Y. Huang, et al., Facile synthesis of α-Fe2O3 nanodisk with superior photocatalytic performance and mechanism insight, Sci. Technol. Adv. Mater. 16 (1) (2015) 14801.
[17] A. Arastehnodeh, M. Saghi, M. Khazaei Nejad, Preparation, characterization and application of nanospherical α-fe2o3 supported on silica for photocatalytic degradation of methylene blue, Iran. J. Chem. Chem. Eng. 38 (2) (2019) 21–28.
[18] J. Huang, M. Yang, C. Gu, M. Zhai, Y. Sun, J. Liu, Hematite solid and hollow spindles: selective synthesis and application in gas sensor and photocatalysis, Mater. Res. Bull. 46 (8) (Aug. 2011) 1211–1218.
[19] X.H. Vu, L.H. Phuoc, N.D. Dien, T.T.H. Pham, L.D. Thanh, Photocatalytic degradation of methylene blue (MB) over α-Fe 2 O 3 nanospindles prepared by a hydrothermal route, J. Electron. Mater. (August, 2019).
[20] A. Muthukrishnaraj, S. Vadivel, V.P. Kamalakannan, N. Balasubramanian, α-Fe2O3/reduced graphene oxide nanorod as efficient photocatalyst for methylene blue degradation, Mater. Res. Innovat. 19 (4) (2015) 258–264.
[21] K. Singh Twinkle, S.A. Bansal, S. Kumar, Graphene oxide (GO)/Copper doped Hematite (α -Fe2O3) nanoparticles for organic pollutants degradation applications at room temperature and neutral pH, Mater. Res. Express 6 (11) (Sep. 2019) 115026.
[22] R. Satheesh, K. Vignesh, A. Suganthi, M. Rajarajan, Visible light responsive photocatalytic applications of transition metal (M = Cu, Ni and Co) doped α-Fe2O3 nanoparticles, J. Environ. Chem. Eng. 2 (4) (2014) 1956–1968.
[23] S.K. Srikar, D.D. Giri, D.B. Pal, P.K. Mishra, S.N. Upadhyay, Green synthesis of silver nanoparticles: a review, Green Sustain. Chem. 6 (1) (2016) 34–56.
[24] Y. Mine, Recent advances in the understanding of egg white protein functionality, Trends Food Sci. Technol. 6 (7) (Jul. 1995) 225–232.
[25] R. Suresh, et al., Synthesis of Co2+-doped Fe2O3 photocatalyst for degradation of pararosaniline dye, Solid State Sci. 68 (Jun. 2017) 39–46.
[26] A. Sharfalddin, E. Alzahrani, M. Alamoudi, Micro, sono, photocatalytic degradation of eosin B using ferric oxide doped with cobalt, Am. Chem. Sci. J. 13 (3) (2016) 1–13.
[27] A. Elyacoubi, A. Rkhaila, B. Sallek, B. Chafik El idrissi, Antibacterial and photocatalytic performances of silver orthophosphate/Hydroxyapatite Composite, Mediterr. J. Chem. 8 (4) (2019) 320–327.
[28] R.M. Cornell, U. Schwertmann, Electronic, electrical and magnetic properties and colour, Iron Oxides (2004) 111–137.
[29] Z. Kaiwen, W. Xuehang, W. Wenwei, X. Jun, T. Siqi, L. Sen, Nanocrystalline LaFeO3 preparation and thermal process of precursor, Adv. Powder Technol. 24 (1) (Jan. 2013) 359–363.
[30] N.T. Hahn, C. Buddie Mullins, Photoelectrochemical performance of nanostructured Ti- and Sn-doped α-Fe2O3 photoanodes, Chem. Mater. 22 (23) (Nov. 2010) 6474–6482.
[31] H.K. Dunn, J.M. Feckl, A. Müller, D. Fattakhova Rohlfing, S.G. Morehead, J. Roos, L.M. Peter, C. Scheu, T. Bein, Tin doping speeds up hole transfer during light-driven water oxidation at hematite photoanodes, Phys. Chem. Chem. Phys. 16 (2014) 24610–24620.
[32] S. Shen, C.X. Kronawitter, J. Jiang, S.S. Mao, L. Guo, Surface tuning for promoted charge transfer in hematite nanorod arrays as water-splitting photoanodes, Nano Res. 5 (2012) 327–336.
[33] R. Beranek, H. Kisch, Tuning the optical and photoelectrochemical properties of surface-modified TiO2, Photochem. Photobiol. Sci. 7 (1) (2007) 40–48.
[34] Y. Yin, X. Zhang, C. Sun, Transition-metal-doped Fe2O3 nanoparticles for oxygen evolution reaction, Prog. Nat. Sci. Mater. Int. 28 (4) (Aug. 2018) 430–436.
[35] P. Mallick, B.N. Dash, X-ray diffraction and UV-visible characterizations of α-Fe2O3 nanoparticles annealed at different temperature, Nanosci. Nanotechnol. 3 (5) (2013) 130–134.
[36] H. Li, et al., Photocatalytic degradation of gaseous toluene over hollow 'spindle-like' α-Fe2O3 loaded with Ag, Mater. Res. Bull. 47 (6) (Jun. 2012) 1459–1466.
[37] Zakaria Anfar, Mohamed Zbair, Hassan Ait Ahsiane, Amane Jada, Noureddine El alem, Microwave assisted green synthesis of Fe2O3/biochar for ultrasonic removal of nonsteroidal antiinflammatory pharmaceuticals, RSC Adv. 19 (2020).
[38] J. Cheng, et al., Highly efficient removal of methylene blue dye from an aqueous solution using cellulose acetate nanofibrous membranes modified by polydopamine, ACS Omega 5 (10) (Mar. 2020) 5389–5400.
[39] F. Allawi, A.M. Juda, S.W. Radhi, Photocatalytic degradation of methylene blue over MgO/α-Fe2O3nano composite prepared by a hydrothermal method, AIP Conf. Proc. 2290 (2020) 30020.
[40] A. Krishnan, P.V. Vishwanathan, A.C. Mohan, R. Panchami, S. Viswanath, A.V. Krishnan, Tuning of photocatalytic performance of CeO2-Fe2O3 composite by Sn-doping for the effective degradation of methlene blue (MB) and methyl orange (MO) dyes, Surface. Interfac. 22 (Feb. 2021) 100808.
[41] D. Pathania, S. Sharma, P. Singh, Removal of methylene blue by adsorption onto activated carbon developed from Ficus carica bast, Arab. J. Chem. 10 (Feb. 2017) S1445–S1451.
[42] S. P. Keerthana *et al.*, "A strategy to enhance the photocatalytic efficiency of α-Fe2O3," Chemosphere, vol. 270, 2021.
[43] N. Popov, et al., Influence of low-spin Co3+ for high-spin Fe3+ substitution on the structural, magnetic, optical and catalytic properties of hematite (α-Fe2O3) nanorods, J. Phys. Chem. Solid. 152 (November 2020) 2021.
[44] N. Popov, et al., Influence of Sn doping on the structural, magnetic, optical and photocatalytic properties of hematite (α-Fe2O3) nanoparticles, J. Phys. Chem. Solid. 161 (Feb. 2022) 110372.
[45] Lagergren, S. K., About the theory of so-called adsorption of soluble substances, Sven. Vetenskapsakad. Handingarl 24 (1898) 1–39 [Online]. Available: http://ci.nii.ac.jp/naid/10016440244/en/. (Accessed 14 November 2021).
[46] S. Sivalingam, T. Kella, M. Maharana, S. Sen, Efficient sono-sorptive elimination of methylene blue by fly ash-derived nano-zeolite X: process optimization, isotherm and kinetic studies, J. Clean. Prod. 208 (Jan. 2019) 1241–1254.
[47] H. Koyuncu, A.R. Kul, Removal of methylene blue dye from aqueous solution by nonliving lichen (Pseudevernia furfuracea (L.) Zopf.), as a novel biosorbent, Appl. Water Sci. 10 (72) (2020).
[48] S. Noreen, et al., Iron oxide (Fe2O3) prepared via green route and adsorption efficiency evaluation for an anionic dye: kinetics, isotherms and thermodynamics studies, J. Mater. Res. Technol. 9 (3) (May 2020) 4206–4217.
[49] V. Vimonses, S. Lei, B. Jin, C.W.K. Chow, C. Saint, Kinetic study and equilibrium isotherm analysis of Congo Red adsorption by clay materials, Chem. Eng. J. 148 (2–3) (May 2009) 354–364.
[50] M. Zbair, K. Ainassaari, A. Drif, et al., Toward new benchmark adsorbents: preparation and characterization of activated carbon from argan nut shell for bisphenol A removal, Environ. Sci. Pollut. Res. 25 (2018) 1869–1882.
[51] W. Zhao, W. Ma, C. Chen, J. Zhao, Z. Shuai, Efficient degradation of toxic organic pollutants with Ni2O3/TiO2-xBx under visible irradiation, J. Am. Chem. Soc. 126 (15) (Mar. 2004) 4782–4783.
[52] N. Prasad, B. Karthikeyan, Cu-doping and annealing effect on the optical properties and enhanced photocatalytic activity of ZnO nanoparticles, Vacuum 146 (Dec. 2017) 501–508.
[53] S. Vadivel, M. Vanitha, A. Muthukrishnaraj, N. Balasubramanian, Graphene oxide–BiOBr composite material as highly efficient photocatalyst for degradation of methylene blue and rhodamine-B dyes, J. Water Proc. Eng. 1 (Apr. 2014) 17–26.